PhD Research Proposal: Molecular Level Design of Nanoporous Lyotropic Liquid Crystal Membranes for Aqueous Separations

Advisors: Michael Shirts and Richard Noble

Benjamin J. Coscia

May 9, 2019

1 State of the Art

Commercial Membranes for Small Molecule Separations

More highly selective nanoporous membranes would be useful for performing complex aqueous separations with seawater and various types of wastewater. For example, sodium chloride and boron in seawater[1] and organic micropollutants found in municipal and industrial wastewaters[2] represent a small subset of the diverse contaminants of water sources. By efficiently separating contaminants from feed solutions with highly selective membranes, it is possible to reduce the number of required membrane passes and post-treatment steps needed for a given filtration process,[3] thus lowering energy requirements and cost. Additionally, one can extract valuable resources from the feed streams. For example, flowback water produced during hydraulic fracturing of shale formations contains dissolved species like acetate whose extraction has economic value.[4]

Reverse osmosis (RO) and nanofiltration (NF) are two prevailing commercial membrane filtration processes that can be used to separate solutes on the order of 1 nm in size and smaller, including ions. Both apply hydraulic pressure to the feed solution in order to overcome osmotic pressure and force water and unfiltered components through the membrane. RO membranes are typically thin film composite with a porous mechanical support layer and a thin but dense polymer matrix active layer where separations occur.[5] RO separates solutes based on the solute's ability to dissolve into and diffuse through the tortuous pathways available in the membrane's dense active layer. RO offers high selectivity at the cost of relatively high energy requirements since one must apply hydraulic pressure on the order of 50–100 bar to the feed solution in order to achieve an economical flux.[6] In contrast to RO membranes, NF membranes have explicit pores on the order of 1 nm in size. Typically, separations are achieved based on size exclusion and Donnan exclusion if the membrane's surface has a net charge.[7] NF membranes require significantly less applied pressure in order to achieve solute flux comparable to RO. Unfortunately, conventional NF membrane synthesis processes, such as phase-inversion,[8] are stochastic in nature which yields pores that are polydisperse in size.[3] Pore size polydispersity is detrimental to membrane selectivity.

The downfall of RO and NF membranes can be summarized by the well-known permeability-selectivity tradeoff. Namely, it is difficult to increase the permeability of a desired molecular or atomic species, while maintaining the same retention of an undesired species.[3]

Nanostructured Membranes

Nanostructured membranes attempt to overcome the permeability-selectivity tradeoff through intelligent design at the molecular level. Graphene sheets, carbon nanotubes (CNTs) and zeolites are three highly studied nanostructured technologies.

Ultrathin-film graphene and graphene oxide membranes are a very active area of research because they offer potential for extremely high permeability membranes. An ideal graphene membrane is a 2D material composed of a single layer of graphene.[9] Synthesis of a single layer of graphene at a large scale without

introducing defects is a challenge that has not yet been overcome. Multilayered graphene membranes are potentially easier to synthesize and more scalable which has resulted in an increasing interest over recent years.[10,11]

Carbon nanotubes (CNTs) have shown promise as aqueous separations membranes due to unprecedentedly fast water transport.[9,12] Practically, dispersing CNTs into a polymer matrix is extremely difficult because they tend to agglomerate due to Van der Waals forces. Functionalization of the CNT walls has been heavily investigated as a way to overcome this issue, however alignment of the CNTs into an array feasible as a nanoporous membrane persists as a challenge to CNT membranes.[13]

Zeolite-coated ceramic membranes offer the potential for permeabilities comparable to ultrafiltration, molecular sieves with pores up to 100 nm in size,[3] with selectivities as good as NF and RO. Zeolites have highly uniform nm-sized crystalline structures with cage-like cavities that allow movement and trapping of small solutes. The crystalline frameworks are typically formed by networks of silicon and aluminum each attached to 4 oxygen atoms in a tetrahedral arrangement.[14] One can replace the silicon and aluminum atoms via ion exchange in order to control the size of the cavities and hence its molecular-seiving properties.[15] A number of studies have tested the permeability and sodium salt rejection of various zeolite membranes, however none have fully overcome the permeability-selectivity tradeoff.[16]

Lyotropic Liquid Crystal Membranes

Preliminary evidence has shown that cross-linked lyotropic liquid crystal (LLC) membranes can be produced at moderate scale and may be capable of performing highly selective separations. LLCs are amphiphilic molecules that have the ability to self-assemble into porous nanostructures[17] that can be cross-linked to create mechanically strong membrane films with periodic uniform-sized pores on the order of 1 nm in diameter.[18] Since LLC polymer membranes lack an appreciable pore size distribution, they inherently exhibit high selectivity due to their molecular weight cut-off (MWCO).[18] Additionally, LLC monomers can be salts, and therefore lead to Donnan exclusion of ions at the membrane-feed solution interface.[7]

The feasibility of nanostructured LLC polymer membranes for selective separations has been demonstrated using LLC monomers that form the type 1 bicontinuous cubic (Q_I)[19–21] and the inverted hexagonal (H_{II}) phases (see Figure 1).[18] When separating organic solutes from NaCl, Q_I-phase membrane filtration experiments have shown selectivity 2–3 times higher than commercial RO and 6–12 times higher than commercial NF membranes.[4] When separating a series of various sized dyes, an H_{II}-phase LLC membrane showed complete rejection of dyes bigger than 1.2 nm in size.[18]

Q_I-phase membranes consist of a tortuous network of three dimensionally interconnected pores that prevent optimal through-plane transport. In contrast, the densely packed, non-tortuous and uniform sized pores of H_{II}-phase membranes represent the ideal geometry for achieving high solute flux.[22] However, the hexagonally packed LC domains of the H_{II}-phase are generally unaligned, which hurts membrane permeability. This domain scale misalignment had inhibited further development of this technology, and research efforts
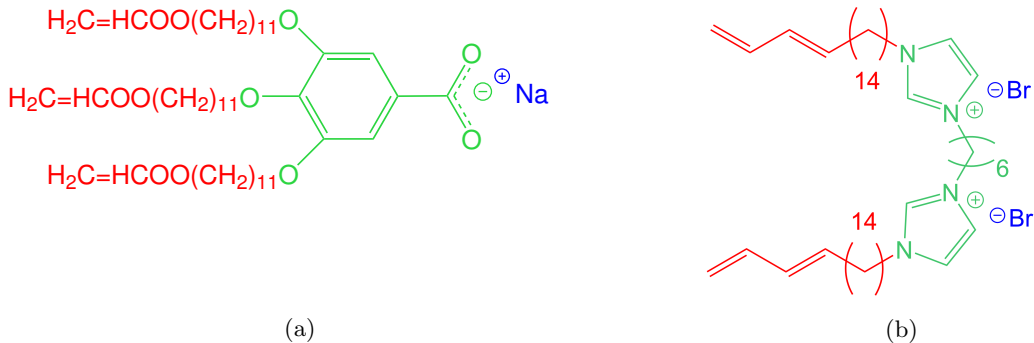
Figure 1: H_{II} and Q_I phase LLC membranes have been synthesized from monomers in (a) and (b) respectively. One can alter membrane properties by modifying the length and number of tails (red), the functional head group (green) and the counterion identity (blue) of LLC monomers.

were focused on the Q_I phase, whose geometry does not require alignment.[23]

Recently, researchers learned how to macroscopically align the hexagonal domains which has revived research into H_{II}-phase LLC polymer membranes. In 2014, Feng et al. showed that one can align Col_h domains, a temperature-dependent hexagonal phase created by neat LLC monomers, using a magnetic field with subsequent cross-linking to lock the structure in place.[24] In 2016, Feng et al. showed that one could also obtain the same result by confining the neat monomer between PDMS or glass substrates since hexagonal mesophases preferentially anchor perpendicular to both surfaces.[25]

Unfortunately, reproducing the work of Feng et al. with the hydrated H_{II} phase has been an experimental challenge. Therefore, the primary focus of experimental research efforts has been with the Q_I phase.

2 Project Objectives

Our current understanding of the molecular details of LLC membranes' nanostructure is not sufficient to be able to precisely design them for specific separations. Dischinger et al. attempted to use an empirical model that correlates the physicochemical properties of the counterion used in a Q_I-phase LLC membrane to solute rejection. Although there was some agreement with their empirical model, it does not offer a sufficiently detailed explanation of the critical molecular interactions leading to the observed behavior.[26] H_{II}-phase LLC polymer membrane studies have been limited primarily to the Na-GA3C11 monomer (Figure 1a) with some characterization done after minor monomer structural modifications. These studies emphasized large scale structural features such as pore spacing as well as size-based rejection.[18, 27] Given the similar topology of H_{II} and Q_I membrane pores, we expect the H_{II} phase will also be subject to complex solute-membrane interactions that are not easily explained by an empirical model.

A molecular-level understanding of structure and transport in LLC polymer membranes, enabled by molecular dynamics (MD) simulations, can provide guidelines to reduce the large chemical space available to design monomers for creation of separation-specific membranes. Using a sufficiently accurate molecular model, we can observe transport of solutes within LLC membrane nanopores with atomistic resolution and

infer mechanisms. Based on this information we will have a much greater capability to intelligently design new membranes by screening new liquid crystal monomer designs with MD simulations. The principles learned can be implemented and tested experimentally.

There are four primary objectives of this PhD research.

1. Develop techniques to build and understand the nanoscopic structure of LLC membranes.

   A useful molecular-level model should incorporate a detailed picture of the nanoscopic pore structure, which is crucial to understanding the role of monomer structure in solute transport and membrane design. I have created a maximally consistent structural model by comparing simulated X-ray diffraction (XRD) patterns, generated from MD trajectories, to an experimental 2D wide angle X-ray scattering (WAXS) spectrum of a Col_h phase LLC membrane. I have used this model as an example in order to understand the ease with which we can apply our approach to alternate monomers and other LC phases.

2. Determine dominant solute-membrane interactions that give rise to transport mechanisms.

   I observed the transport of a relatively large set of small polar solutes placed within the H_{II} phase membrane nanopores. I analyzed the time series of each solute's position in addition to directly measuring the physical interactions, such as hydrogen bonding and ion coordination, between solutes and LLC monomers.

3. Create a stochastic model which can project long timescale transport behavior.

   I will combine my qualitative knowledge of the solute transport mechanisms with simulation data in order to inform a stochastic model. This model should closely reproduce the properties of the time series that we observe in our simulations. Due to the low computational cost of a stochastic model relative to MD simulations, I will be able to forecast long timescale transport behavior and make well-converged predictions of macroscopic transport properties.

4. Adapt the same analysis to the Q_I phase.

   Over the course of this project, experimental research surrounding LLC membranes has shifted nearly all focus towards the Q_I phase due to its more facile synthesis. Although most of my work has been applied to the H_{II} phase, much of the same analyses can be applied to the Q_I phase. The biggest challenge will be adapting my techniques to its more complex three dimensional geometry.

3   Progress to Date

Objective 1: Build and understand the nanoscopic structure of the H_{II} phase (Complete)

My first task was to develop a procedure for building and equilibrating an atomistic LLC membrane system (see Figure 2). I chose to build a monoclinic unit cell consisting of four pores. Each pore is composed

of monomer columns, where each column consists of 20 monomers stacked on top of each other so that the phenyl groups are coplanar with each other and the xy plane. The columns are oriented so that the hydrophilic monomer head groups face towards the pore center. I did not add any water to the initial configuration because I compared the structure to experimental data for a system claimed to be synthesized with only neat monomer. I equilibrated unit cells using a series of simulations with head groups held in place by position restraints, gradually reducing the force constant of the position restraints until the system was completely unrestrained. I let the system equilibrate for 400 ns of simulation time.

(a)   (b)   (c)
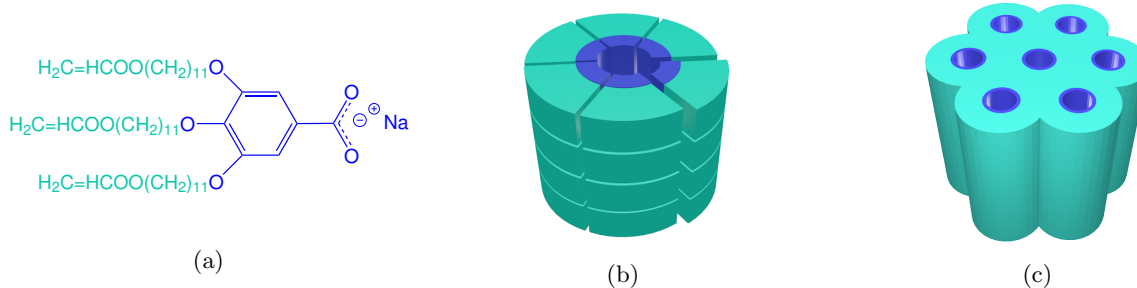
Figure 2: (a) The LLC monomer Na-GA3C11 exhibits wedge-like character. (b) Monomers stack on top of each other to create columns with short range order, then assemble into pores with hydrophilic head groups (blue) facing towards the pore center. (c) The pores assemble into hexagonally packed columnar mesophases.

I evaluated a number of different initial column architectures. I stacked monomers in parallel displaced and sandwiched configurations, two possible π-π stacking modes.[28] I also varied the initial distance between stacked monomers, d. I chose d values of 3.7 Å, based on experimental WAXS measurements, as well as 5 Å as a test of its sensitivity.

My model's geometry is most consistent with experiment for systems built with 5 columns per pore and monomers initially stacked 3.7 Å apart (see Figure 3). I equilibrated systems with 4, 5, 6, 7 and 8 columns per pore. The pore spacing of 5 column-per-pore systems agree well with experiment. 6 column-per-pore systems built with $d = 5$ Å appear to yield an experimentally consistent pore spacing however, the equilibrated distance between stacked monomers stay close to 5 Å which is inconsistent with experiment. In general, the equilibrated distance between monomers stays close to its initial value.
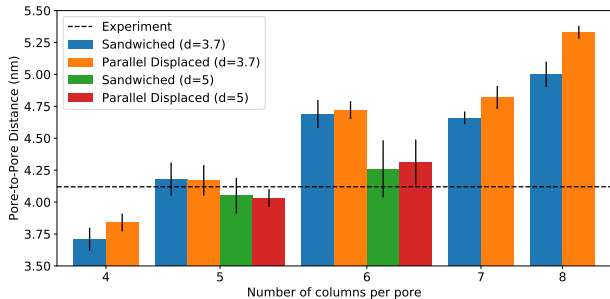

Figure 3: Systems with 5 columns per pore have equilibrated pore spacings closest to the experimental value of 4.12 nm. The equilibrated pore spacing of the model increases as the number of columns in each pore increases.

I further validated the structure of our molecular model by verifying its consistency with five major reflections present in the experimental WAXS pattern. Using MD trajectories, we simulated X-ray diffraction (XRD) patterns that we could compare to the WAXS data by taking the appropriate cross-section of the time-averaged 3D structure factor. The five major reflections and the structural features leading to them are summarized and described in the

caption of Figure 4. None of the models simulated to this point could reproduce R-double.

It is necessary to add a small amount of water to the model in order to fully reproduce all features of the WAXS pattern (see Figure 4b). I obtain the most experimentally consistent structure when I build systems in the parallel displaced configuration with 1 wt% water added to the pores. This is the only configuration that gives rise to the R-double feature. R-double appears because vertically adjacent monomer head groups hydrogen bond with shared water molecules, causing them to be drawn closer together. When multiple pairing interactions occur in series along the same pore axis, the center of masses of the pairs are spaced apart at twice the π-stacking distance. The necessity of water in my model suggests that the membrane synthesized by Feng et al. was slightly hydrated due to water molecules leached from surroundings by the hydroscopic monomers. Similar suspicions have been voiced by experimentalists in unpublished communications.

On the timescales that we can reasonably simulate, our model exhibits slow dynamics. Consequently, there are very few uncorrelated frames in our trajectories which leads to noise and sharpened reflections in the simulated XRD patterns. We can overcome this issue by combining the structure factors generated from an ensemble of trajectories produced starting from an ensemble of uncorrelated initial configurations.

The composition of the pores does not change regardless of which
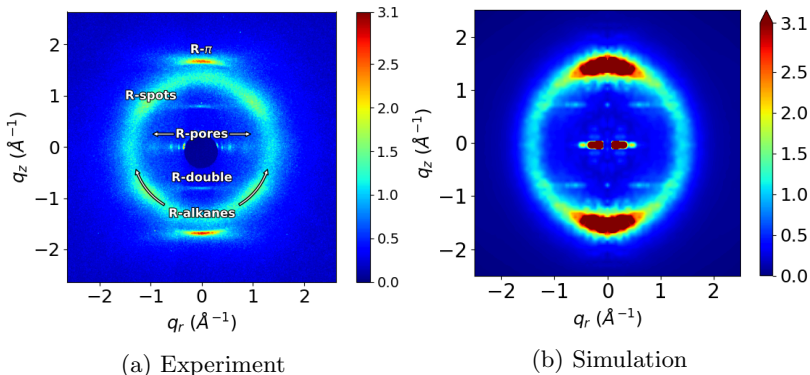

(a) Experiment   (b) Simulation

Figure 4: (a) 2D-WAXS gives details about repeating features on the order of angstroms. Explanations for each of the 5 major reflections present are as follows: (R-π) Aromatic head groups $\pi - \pi$ stack 3.7 Å apart. (R-double) Monomer head groups associate into pairs by hydrogen bonding with a shared water molecule. (R-alkanes) Alkane chain tails pack 4.5 Å apart. (R-spots) Monomer tails pack hexagonally. (R-pores) The pores are spaced 4.12 nm apart and pack hexagonally. (b) We obtain a maximally consistent match between simulated XRD patterns and experimental WAXS data when we build systems in the parallel displaced configuration with 1 wt % water included in the pores.

initial configuration we study. In Figure 5, we plot the radial density of various monomer components as a function of distance from the pore centers. All are qualitatively similar meaning that a solute placed in any of these systems should experience a similar chemical environment. Although we will move forward with our most promising configuration, this is an important finding since it implies that we do not need to apply the same level of rigor when screening new monomers.

My work towards this objective is published in the Journal of Physical Chemistry B: Coscia et al. *J. Phys. Chem. B*, 123, 289-309 (2019).

Objective 2: *Determine transport mechanisms* (Complete)

We added additional water to our most experimentally consistent structural model in order to create a higher water content H_{II} phase model. Researchers have synthesized the H_{II} phase using the NaGA3C11 monomer with water contents ranging from 7 - 20 wt%, with 10 wt% being the most common.[17,18] However,

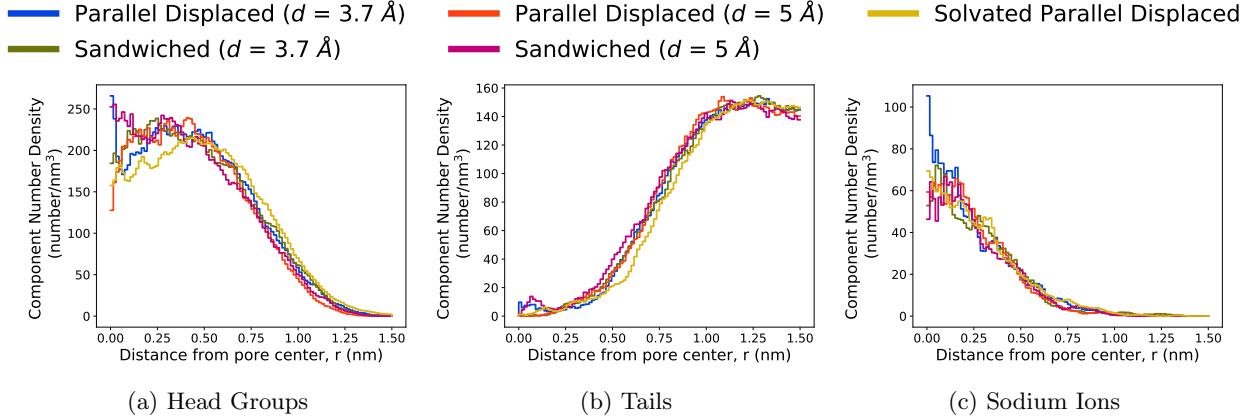(a) Head Groups   (b) Tails   (c) Sodium Ions

Figure 5: In all systems studied, the component radial distribution functions are similar. They exhibit a composition gradient transitioning from the hydrophilic to the hydrophobic regions. The biggest differences are at r=0 where noise is higher due to decreased sampling. The center of the pore is not hollow, but contains sodium ions and head groups, even when the system is solvated. This architecture may impede transport in the real system in a chemically-dependent manner. The solvated system has a lower density of head groups near the pore center which is likely due to the swelling that is necessary in order to fit water molecules in the pore region.

Resel et al. stated that the system is likely fully hydrated at 7 wt % water with additional water trapped in defects between mesophases.[27] Consequently, we chose to build two systems with 5 and 10 wt% water.

(a) 5 wt% water   (b) 10 wt% water
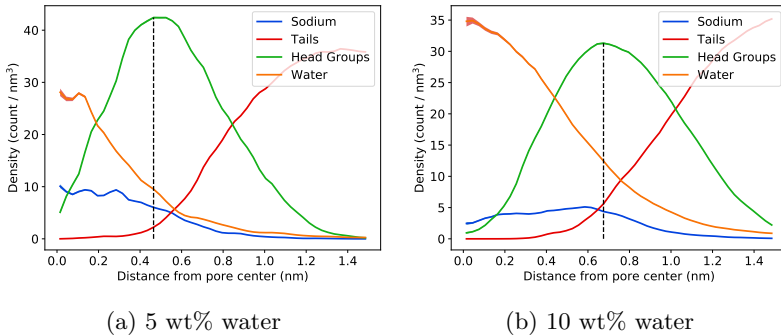
Figure 6: The radial densities of various monomer components paint a picture of the pore topology where the pore centers are primarily composed of water and sodium ions. The monomer groups labeled in each plot correspond to the color-coded monomer pictured in Figure 1a. All RDFs represent the number of atoms located at a given distance from the pore center normalized by the volume of the annular bin to which they belong. The black dashed lines are positioned so that they intersect with the maximum head group density. (a) In the 5 wt % system, monomer head groups are situated about 0.45 nm from the pore center. Sodium and water are densest near the pore center (b) Monomers in the 10 wt % system retreat an additional 0.2 nm to make room for more water. Water is densest at the pore center, but sodium ion density peaks closer to the head groups since many stay bound to carboxylate groups.

Upon simulating each system, we observed that water partitions into the distal tail region. Based on the radial distance from the pore center where the minimum water density occurs, we defined the distal tail region to be greater than 1.5 nm from any pore center. There is approximately a 3:2 ratio of water in the pores to water in the distal tails. Due to the wedge shape of the monomers, the distal tail region has a relatively low density leaving space for water molecules to fill.

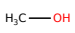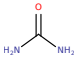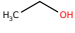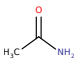The pores of the H_{II} phase are primarily a mixture of water and sodium ions. The maximum density of head groups occurs 0.45 and 0.65 nm from the pore center in the 5 and 10 wt% water systems respectively (see Figure 6). There are almost no head groups occupying the pore center.

Water and sodium transport is significantly faster in the less crowded 10 wt% water pores. The mean
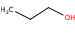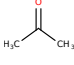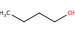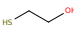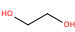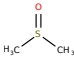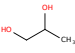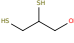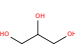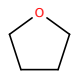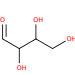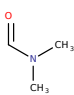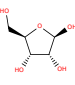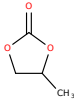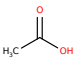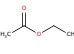
Solute Name	Abbreviation	Structure	Solute Name	Abbreviation	Structure
methanol	MeOH		urea	URE	
ethanol	EtOH		acetamide	AcN	
propanol	PrOH		acetone	ACE	
butanol	BtOH		mercaptoethanol	ME	
ethylene glycol	EG		dimethyl sulfoxide	DMSO	
propylene glycol	PG		2,3-dimercapto-1-propanol	DMP	
glycerol	GLY		tetrahydrofuran	THF	
tetrose	TET		dimethylformamide	DMF	
ribose	RIB		propylene carbonate	PC	
acetic acid	AcOH		ethyl acetate	EAC	

Figure 7: The solutes studied in this work along with the abbreviations used in subsequent figures and their chemical structures. Solutes are color-coded according to similarities in their structure. Blue corresponds to simple alcohols, red to diols, triols and sugars, green to ketone-like solutes, orange to sulfur-containing solutes and yellow to solutes that can only accept hydrogen bonds but not donate.

squared displacement (MSD) of water is about 51 times higher and the MSD of sodium is about 49 times higher compared to the 5 wt% system. In general we observe similar solute transport mechanisms in the 5 and 10 wt% water systems but on different time scales.

We observed transport of 20 different small polar solutes in the pores of our model. We created a separate initial configuration for each solute studied and placed 6 solutes, equally spaced in z, in each nanopore. After a 5 ns equilibration, we allowed the solutes to simulate for 1 microsecond.

The solute MSDs are not a monotonic function of solute size. In Figures 8a and 8b, we plot the average MSD of each solute. In Figure 8c and 8d, we plot solute MSDs against their molecular radius. We also show theoretical curves which illustrate the expected MSD of each solute if they were to travel unhindered. We ensured that the Stokes-Einstein equation with the correction factor of Gierer and Wirtz[29] passed through methanol's MSD and radius in order to give an approximate frame of reference. The correction factor attempts to include the effects of microfriction that begin to play a role when solute size becomes on the order of solvent size. Since methanol is small, we assume that it travels unhindered relative to all other solutes. The theoretical line serves as an approximate boundary between subdiffusive, Brownian and superdiffusive behavior. In the majority of cases, solute MSDs fall well below the theoretical lines and therefore are subject

to more hindrance than methanol due to factors other than size.

Intermittent hops between long periods of entrapment lead to sub-diffusive solute transport behavior. As implied by Figures 8d and 8c, most solutes move significantly slower than expected. In Figure 9a, we've plotted the z-direction trajectory of three ethanol molecules. Typically, long periods of entrapment occur when ethanol molecules are far from the pore center, while there is a much greater degree of mobility close to the pore center. The MSD curve averaged over all ethanol trajectories is shown in Figure 9b. The curve is sub-linear and thus subdiffusive.

Due to the crowded environment

(a) 5 wt % water

(b) 10 wt % water

(c) 5 wt % water

(d) 10 wt % water

Figure 8: The MSDs of solutes in the 5 wt % water system (a) are significantly smaller than those of the solutes in the 10 wt % water system (b). The MSDs are not a monotonic function of molecular size (c and d). A significant number of solute MSDs fall below the theoretical lines predicted by the Stokes-Einstein equation and Gierer and Wirtz' corrected Stokes-Einstein equation.

among the monomer tails, solutes generally move faster in the less dense pore region. Figure 10a shows that this is the case for all solutes. Hops made in the pore region are on average 59 % larger than those made outside the pore region.
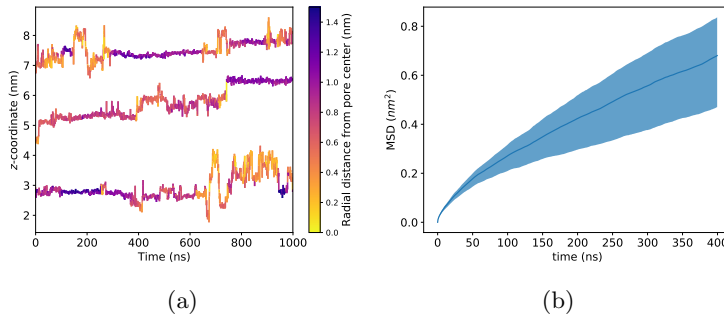

(a)

(b)

Figure 9: All solutes show subdiffusive transport behavior inside the membrane's nanopores, similar to that exhibited by ethanol. (a) The z-coordinate trace of 3 representative ethanol COMs shows clear periods of entrapment separated by hops. In general, the longest dwell times occur when solutes are situated far from the pore center and the hops occur when solutes are close to the pore center. (b) The time-averaged MSD of ethanol is sub-linear which suggests transport is governed by an anomalous subdiffusion process.

However, time spent in the pore region does not necessarily result in a high MSD. For example, ribose spends the largest fraction of time in the pore region, but has the fifth lowest hop frequency and the third lowest average MSD (see Figures 10b and 10c). Therefore, proximity to the pore center cannot be the sole variable that determines transport properties.

Among the set of solutes studied, we observe three different mechanisms of entrapment that are responsible for subdiffusive behavior:

Figure 10: (a) Hops made in the pore region of the 10 wt% water system are, on average, 59 % larger than those made outside the pore region. The trend in hop lengths is similar to the trend in MSDs shown in Figure 8b implying that solutes which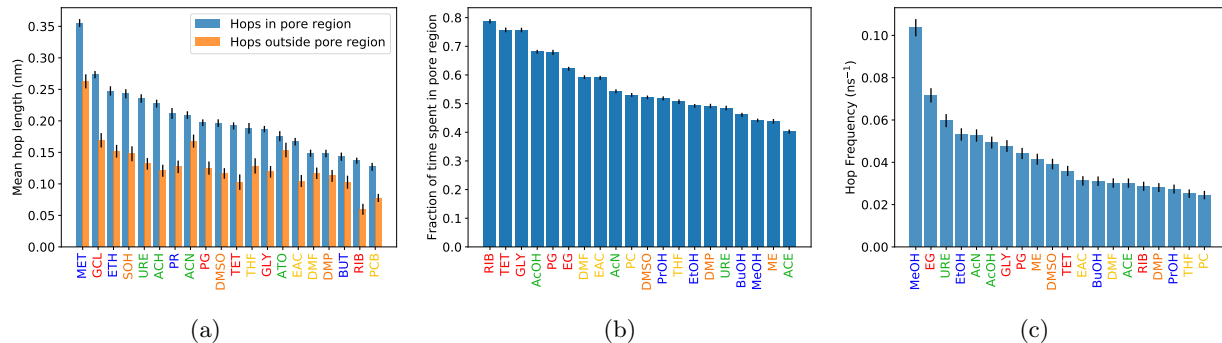 make consistently larger hops have higher MSDs. The fraction of time spent by a solute in the pore region (b) does not necessarily lead to more frequent hopping (c). For example, ribose spends the largest fraction of time in the pore region, yet performs the the fifth lowest number of hops.

1. As already demonstrated by Figures 9a and Figure 10a, solutes that drift away from the pore center can become entangled in the monomer tails.

2. Many of the solutes we studied are capable of donating hydrogen bonds to monomer head groups and thus are prone to temporary immobilization through this interaction.

3. Because all solutes are polar, they have regions of concentrated electron density, modeled as partial charges, which can associate with sodium ions bound to monomer head groups.
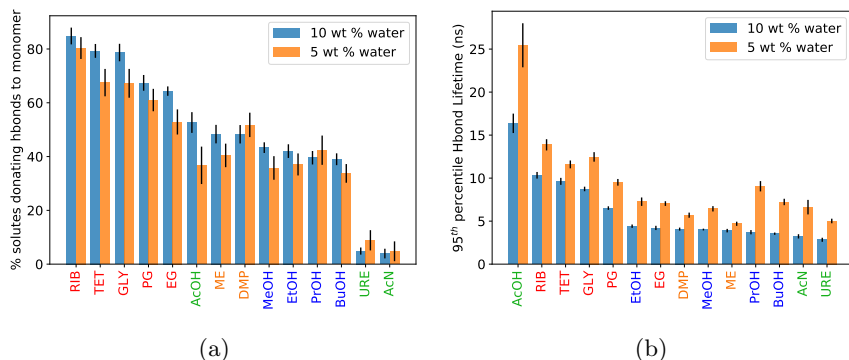

Figure 11: (a) Solutes capable of donating hydrogen bonds to monomer head groups do so to varying degrees. The reported percentages represent unique solute-monomer hydrogen bonds. Individual solutes that hydrogen bond with multiple head groups simultaneously are only counted once. (b) The lifetime of individual hydrogen bonds appears correlated to the percentage of solutes involved in hydrogen bond interactions. Hydrogen bond lifetimes tend to be longer for solutes that hydrogen bond frequently. Note that solutes incapable of donating hydrogen bonds are omitted from this figure.

The frequency with which solutes donate hydrogen bonds to monomer head groups is related to the number of hydrogen bond donating atoms as well as their identity. The percentage of solutes actively participating in at least one hydrogen bond with a head group each frame descends as the number of hydroxyl groups decreases (Figure 11a). Solutes with many hydroxyl groups, such as ribose, tetrose

and glycerol, can donate multiple hydrogen bonds to monomer head groups simultaneously. When one hydrogen bond is broken, other hydrogen bonds work to hold the solute in place, which allows broken hydrogen bonds to reform. Solutes containing sulfur and nitrogen atoms in place of oxygen atoms hydrogen bond less

frequently since they are less electronegative elements.[30] The lifetime of hydrogen bonds follows nearly the same trend (Figure 11b). Hydrogen bonds of solutes that hydrogen bond more frequently last longer.

Solutes with carbonyl groups tend to associate with sodium ions most frequently. Nearly all of the most coordinated solutes contain a carbonyl group, except for DMSO which has an analogous sulfinyl group (see Figure 12a). There is a significant drop in sodium ion association for solutes that do not contain carbonyl groups or multiple hydroxyl
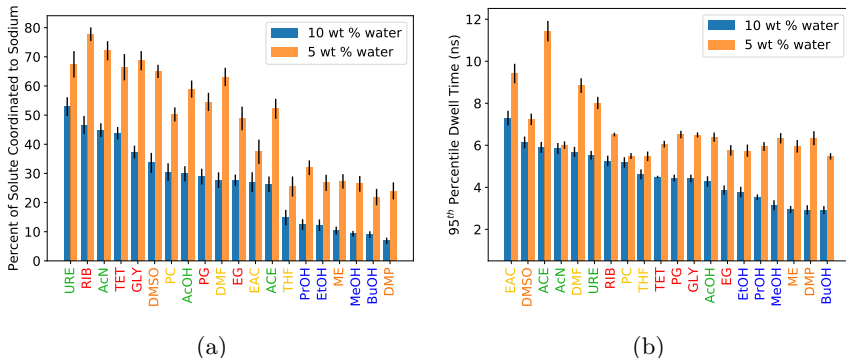

Figure 12: (a) Solutes, especially those with carbonyl groups, spend a significant fraction of time coordinated to sodium ions. (b) The length of time a solute-sodium pairs spends associated tends to be higher for pairs that associate more frequently.

groups to compensate. The corresponding dwell times follow a similar trend, however the dwell times of highly coordinated solutes with multiple hydroxyl groups are generally lower since association between hydroxyl groups and sodium is apparently a weaker interaction (Figure 12b). Solutes with nitrogen atoms adjacent to the carbonyl groups tend to associate with sodium ions significantly more.

A manuscript based on the work presented towards this objective is under review for publication in the Journal of Physical Chemistry B.

Figure 13: The movement of solutes may be well-described by an sFBM process which can be simulated using parameters that describe the solute's hop lengths, dwell times and degree of correlation between hops. Here I use the parameters derived from ethylene glycol as an example. (a) The distribution of hop lengths made by ethylene glycol appears Gaussian, which can be described by the maximum likelihood estimate (MLE) of the σ parameter, with assumed mean, μ, of 0. (b) The distribution of dwell times between hops can be fit to a power law whose decay is described by the MLE of the parameter α. (c) Hops are anticorrelated to their previous hop as indicated by the negative value at $k = 1$ of the autocorrelation function, γ. The Hurst parameter, H, is a measure of long term memory of the hops and is directly related to the autocorrelation function of fractional Brownian process.

Objective 3: *Create a stochastic model* (**In Progress**)

While one can clearly learn a great deal of qualitative information about mechanistic behavior on MD-

accessible timescales, my work's impact would greatly increase if I could create a model that could predict macroscopic quantities such as permeability and selectivity within a reasonable degree of certainty. A stochastic model derived from simulation data could achieve this however, there is not a well-defined procedure for this type of extrapolation. Therefore, I am exploring two different approaches towards this end.

Approach 1: subordinated fraction Brownian motion: My first route towards a stochastic model is to simulate realizations of a subordinated fractional Brownian motion (sFBM) process based on parameters extracted from solute time series.[31] As demonstrated by the example in Figures 13a and 13b, hop length distributions in the z-direction appear Gaussian while the distribution of dwell times between hops appears to be distributed according to a power law. Alone, these distributions characterize a continuous time random walk (CTRW), which is a subdiffusive process where particles hop a random distance in a random direction and stay there for a random amount of time.[32] Unlike a CTRW, the hops in our system appear anti-correlated to their previous hop as shown by the autocorrelation function in Figure 13c. A CTRW with anticorrelated hops is well-described by an sFBM process.

Figure 14: The trends in the MSD calculated directly from MD simulations and from realizations of the sFBM process mostly agree, but the sFBM predictions are generally far too low.
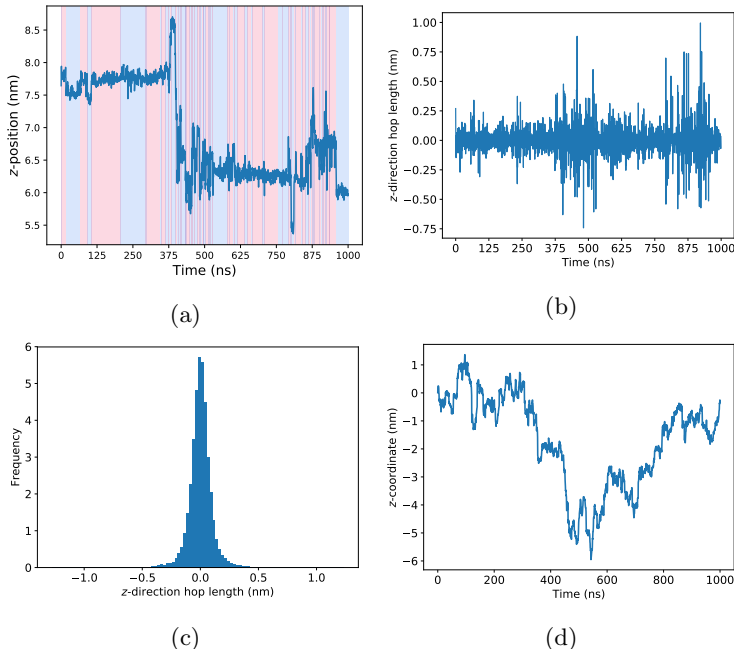

(a)

(b)

(c)

(d)

Figure 15: In contrast to our first approach which relies on accurate detection of hops, density forecasting uses all of the time series information at our disposal. (a) Our first approach identifies hops based on breakpoints, indicated by color transitions. All information is lost between breakpoints. (b) Instead we can calculate hop lengths between each time step and (c) compile them into a single probability density. (d) As a first approximation, one can simulate time series by randomly drawing from the distribution in (c).

Solute MSDs calculated based on realizations of an sFBM process mostly preserve the trends in MSD calculated directly from MD simulations (see Figure 14), but the predictions are generally too low. For each solute, I used the parameters described in Figure 13 to generate $1e4$ realizations of an sFBM process, each with the same length as the MD simulations (1000 ns) so that I could make a direct comparison between their MSDs. While the sFBM MSD prediction for methanol is too high, the rest are on average only 46% of the MD calculated MSD values.

This approach might be improved by incorporating radial dependence into the three sFBM parameters described in Fig-

ure 13. In Figure 10a, we showed that hops by solutes situated inside the pores are 59% larger than hops by solutes in the tails, which leads to two distinct values of σ. Similarly, we can determine radially dependent values of α and H.

A simple two state model, in pore versus out of pore, may be sufficient to fully incorporate radially dependent effects. Based on the fraction of time spent in the pore region (Figure 10b), we can determine the appropriate balance of each type of parameter to use when simulating sFBM realizations. We would also need some kind of switching frequency, or dwell time in each region since it does not make physical sense for a solute to enter and exit the pore region every other time step.

Figure 16: The histogram of z values coming from z_t calculated with Equation 1 appears uniform meaning $p(h)$ is well-sampled by the out-sample data.

If the two state model proves insufficient, I can add increasing levels of complexity. For example, I might make the radial dependence a continuous function, or I could assign parameters that are dependent on the type of trapping mechanism affecting the solute.

Approach 2: density forecasting: Density forecasting can provide predictions based on properties of a time series without any knowledge of the physical interactions leading to those properties.
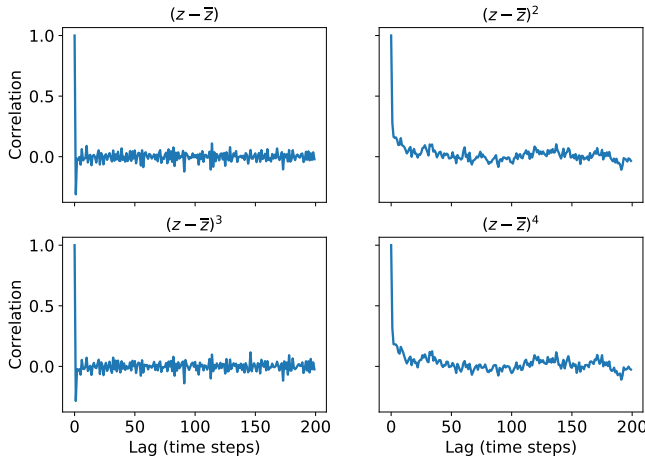

Figure 17: Correlograms of z_t reveal dependence for all 4 powers of $(z - \bar{z})$.

In contrast to the first approach, density forecasting allows one to use all of available trajectory information. In order to construct distributions of hop lengths and dwell times with my first approach, I needed to locate precise time points at which hops occurred. We achieved this using an off-line breakpoint detection algorithm implemented in the python package `ruptures`.[33] The algorithm does a decent job of identifying hops, but still loses information as demonstrated in Figure 15a. With density forecasting, one can instead compile the hop length and magnitude between each time step (Figure 15b) into a probability density like that shown in Figure 15c. As a first attempt, one could randomly draw from this distribution in order to construct a time series like that shown in Figure 15d.

One can test how well a time series of hop lengths, h_t, is described by the hop density, $p(h)$, in Figure 15c using the probability integral transform:[34]
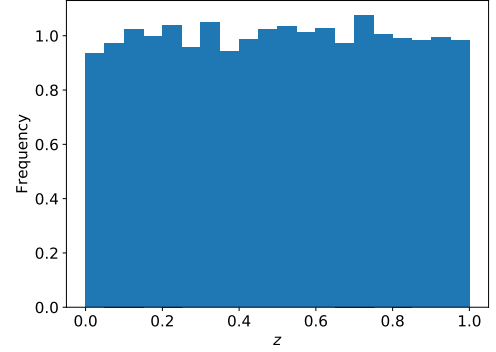
$$z_t = \int_{-\infty}^{h_t} p(u)du \tag{1}$$

13

Generally, one uses the first half of a time series, or in-sample data, to create $p(h)$ and applies Equation 1 to the second half of the time series, or out-sample data. If the distribution of z_t values is uniform, then the cumulative distribution function of $p(h)$ has been sampled uniformly by the out-sample data and there is evidence that the time series is well-described by $p(h)$. Using the out-sample data from Figure 15, we observe a uniform distribution of z_t values (Figure 16).

However, it is also necessary to look for correlations in z_t. Diebold et al. found that examination of the correlograms of $(z - \overline{z})$, $(z - \overline{z})^2$, $(z - \overline{z})^3$ and $(z - \overline{z})^4$, which represent dependence of the mean, variance, skewness and kurtosis respectively, are adequate to identify potentially sophisticated and nonlinear forms of past dependence.[34] Continuing with our example above, the correlograms of z_t shown in Figure 17 exhibit serial dependence for all powers of $(z - \overline{z})$. Our time series exhibits dependence on its past values, a feature that was not included in the forecast shown in Figure 15d.

Going forward, I will need to incorporate previous dependence in the form of a conditional density forecast with the form $p(h|\Omega_t)$ where Ω_t incorporates past hop lengths and radial distances from the pore center. These types of autoregressive models have been widely studied in the context of economics, but are still well-suited for application to solute transport.[35]

Objective 4: *Apply analyses to Q_I phase* (**In Progress**)

Paralleling our work on the H_{II} phase, my first task towards this objective was to build a suitable unit cell representation of the Q_I phase. Unfortunately, the true space group of the Q_I phase that we are studying is unknown. Experimental diffraction has narrowed down the possible bicontinuous cubic configurations to the Ia3d and Pn3m space groups. Therefore, we will build both types of unit cells and search for clues that can be used to differentiate them experimentally.

(a)   (b)
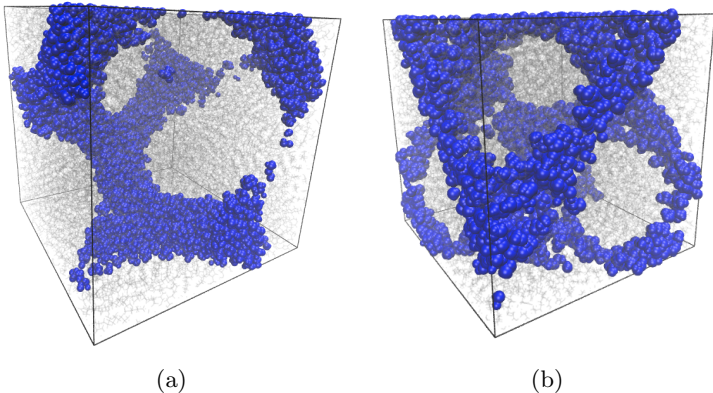
Figure 18: I developed a procedure capable of building both (a) Ia3d and (b) Pn3m unit cells from arbitrary monomers with controllable pore size. The blue glycerol molecules highlight the aqeuous region where transport occurs.

I have developed a procedure that can build both Ia3d and Pn3m unit cells. To our knowledge, nobody has ever built an atomistic bicontinuous cubic phase system without the aid of self-assembly. Self-assembly can be a long process, especially for fully atomistic systems. Instead, we used known analytical equations that describe the surface of these systems in order to place monomers into a unit cell. Monomers are placed perpendicular to the surface in random locations that don't overlap. One can control the pore size by translating monomers perpendicular to the surface at the point where they are attached.

First, I will study the structure of the Q_I phase using methodology similar to that used for the H_{II} phase

I will attempt to identify one of the space groups as the most likely experimental configuration based on simulated XRD signatures, although this might not work due to the known similarity of Ia3d and Pn3m XRD patterns.

Then I will study transport of solutes within these atomistic unit cells, adapting the same analyses used in Objectives 2–3. The primary challenge will be adapting my techniques to the more complex pore geometry of the Q_I phase, however I expect that main conclusions will not deviate far from those of the H_{II} phase since the chemical environments within the nanopores are qualitatively similar.. We may be able to identify which space group is correct if there are significantly different transport properties between systems.

4   Timeline for Completion of Objectives

A schematic of the estimated timeline that I plan to follow for the completion of tasks pertinent to finishing all objectives is given in Table 1. Ideally, each task will become a published manuscript. I will run simulations required to study the structure of the bicontinuous cubic phase in parallel with the continued development of my stochastic model of transport in the H_{II} phase. Simulations and analysis required for Q_I phase solute transport studies analogous to those of Objective 2 will be carried out throughout Fall 2019. Application of a stochastic model to the Q_I phase will be finished by May 2020, just before I defend my dissertation.

TABLE 1   Estimated Timeline for Completion of Objectives

August 2019	Complete Stochastic Model for H_{II} phase
September 2019	Finalize Q_I phase structure
January 2020	Finish transport study of Q_I phase
April 2020	Finish application of stochastic model to Q_I phase
May 2020	PhD Defense

5   Resource Requirements

The remainder of our work will require the use of high performance computing (HPC) resources. We will continue using Bridges, an XSEDE resource as well as Summit, a supercomputer located at CU Boulder.

6   Safety Considerations

Although my work is confined to computer work in an office space, there are associated health risks that I must mitigate. Proper ergonomics ensure maximum comfort and help me to work efficiently. Sitting up straight and having proper back support are necessary to relieve pressure on the discs of my vertebrae. My monitors are positioned an arm's length directly in front of me with the tops of the monitors at eye level in order to reduce head, neck and eye strain. Finally, I take frequent breaks and go for walks around the building.

References

[1] C. Fritzmann, J. Lwenberg, T. Wintgens, and T. Melin, "State-of-the-Art of Reverse Osmosis Desalination," *Desalination*, vol. 216, pp. 1–76, Oct. 2007.

[2] R. P. Schwarzenbach, B. I. Escher, K. Fenner, T. B. Hofstetter, C. A. Johnson, U. v. Gunten, and B. Wehrli, "The Challenge of Micropollutants in Aquatic Systems," *Science*, vol. 313, pp. 1072–1077, Aug. 2006.

[3] J. R. Werber, C. O. Osuji, and M. Elimelech, "Materials for Next-Generation Desalination and Water Purification Membranes," *Nat. Rev. Mater.*, vol. 1, p. 16018, May 2016.

[4] S. M. Dischinger, J. Rosenblum, R. D. Noble, D. L. Gin, and K. G. Linden, "Application of a Lyotropic Liquid Crystal Nanofiltration Membrane for Hydraulic Fracturing Flowback Water: Selectivity and Implications for Treatment," *J. Membr. Sci.*, vol. 543, pp. 319–327, Dec. 2017.

[5] B.-H. Jeong, E. M. V. Hoek, Y. Yan, A. Subramani, X. Huang, G. Hurwitz, A. K. Ghosh, and A. Jawor, "Interfacial Polymerization of Thin Film Nanocomposites: A New Concept for Reverse Osmosis Membranes," *J. Membr. Sci.*, vol. 294, pp. 1–7, May 2007.

[6] B. Van Der Bruggen, C. Vandecasteele, T. Van Gestel, W. Doyen, and R. Leysen, "A Review of Pressure-Driven Membrane Processes in Wastewater Treatment and Drinking Water Production," *Environ. Prog.*, vol. 22, pp. 46–56, Apr. 2003.

[7] F. G. Donnan, "Theory of Membrane Equilibria and Membrane Potentials in the Presence of Non-Dialysing Electrolytes. a Contribution to Physical-Chemical Physiology," *J. Membr. Sci.*, vol. 100, pp. 45–55, Mar. 1995.

[8] C. A. Smolders, A. J. Reuvers, R. M. Boom, and I. M. Wienk, "Microstructures in Phase-Inversion Membranes. Part 1. Formation of Macrovoids," *J. Membr. Sci.*, vol. 73, pp. 259–275, Oct. 1992.

[9] T. Humplik, J. Lee, S. C. OHern, B. A. Fellman, M. A. Baig, S. F. Hassan, M. A. Atieh, F. Rahman, T. Laoui, R. Karnik, and E. N. Wang, "Nanostructured Materials for Water Desalination," *Nanotechnology*, vol. 22, no. 29, p. 292001, 2011.

[10] D. Cohen-Tanugi, L.-C. Lin, and J. Grossman, "Multilayer Nanoporous Graphene Membranes for Water Desalination," *Nano Lett.*, vol. 16, pp. 1027–1033, Jan. 2016.

[11] Y. Wei, Y. Zhang, X. Gao, Z. Ma, X. Wang, and C. Gao, "Multilayered graphene oxide membranes for water treatment: Areview," *Carbon*, vol. 139, pp. 964–981, Nov. 2018.

[12] G. Hummer, J. C. Rasaiah, and J. P. Noworyta, "Water conduction through the hydrophobic channel of a carbon nanotube.," *Nature*, vol. 414, no. 6860, pp. 188–190, 2001.

[13] N. G. Sahoo, S. Rana, J. W. Cho, L. Li, and S. H. Chan, "Polymer nanocomposites based on functionalized carbon nanotubes," *Progress in Polymer Science*, vol. 35, pp. 837–867, July 2010.

[14] S. M. Auerbach, K. A. Carrado, and P. K. Dutta, eds., *Handbook of zeolite science and technology.* New York: M. Dekker, 2003. OCLC: ocm52850544.

[15] Y. Li, T.-S. Chung, and S. Kulprathipanja, "Novel Ag+-zeolite/polymer mixed matrix membranes with a high CO2/CH4 selectivity," *AIChE Journal*, vol. 53, no. 3, pp. 610–616, 2007.

[16] M. Pendergast and E. M.V.Hoek, "A review of water treatment membrane nanotechnologies," *Energy & Environmental Science*, vol. 4, no. 6, pp. 1946–1971, 2011.

[17] R. C. Smith, W. M. Fischer, and D. L. Gin, "Ordered Poly(p-phenylenevinylene) Matrix Nanocomposites via Lyotropic Liquid-Crystalline Monomers," *J. Am. Chem. Soc.*, vol. 119, no. 17, pp. 4092–4093, 1997.

[18] M. Zhou, T. J. Kidd, R. D. Noble, and D. L. Gin, "Supported Lyotropic Liquid-Crystal Polymer Membranes: Promising Materials for Molecular-Size-Selective Aqueous Nanofiltration," *Adv. Mater.*, vol. 17, pp. 1850–1853, Aug. 2005.

[19] E. S. Hatakeyama, C. J. Gabriel, B. R. Wiesenauer, J. L. Lohr, M. Zhou, R. D. Noble, and D. L. Gin, "Water Filtration Performance of a Lyotropic Liquid Crystal Polymer Membrane with Uniform, Sub-1-Nm Pores," *J. Membr. Sci.*, vol. 366, no. 1-2, pp. 62–72, 2011.

[20] E. S. Hatakeyama, B. R. Wiesenauer, C. J. Gabriel, R. D. Noble, and D. L. Gin, "Nanoporous, Bicontinuous Cubic Lyotropic Liquid Crystal Networks via Polymerizable Gemini Ammonium Surfactants," *Chem. Mater.*, vol. 22, pp. 4525–4527, Aug. 2010.

[21] B. M. Carter, B. R. Wiesenauer, E. S. Hatakeyama, J. L. Barton, R. D. Noble, and D. L. Gin, "Glycerol-Based Bicontinuous Cubic Lyotropic Liquid Crystal Monomer System for the Fabrication of Thin-Film Membranes with Uniform Nanopores," *Chem. Mater.*, vol. 24, pp. 4005–4007, Nov. 2012.

[22] M. Matyka, A. Khalili, and Z. Koza, "Tortuosity-Porosity Relation in Porous Media Flow," *Phys. Rev. E*, vol. 78, p. 026306, Aug. 2008.

[23] M. Zhou, P. R. Nemade, X. Lu, X. Zeng, E. S. Hatakeyama, R. D. Noble, and D. L. Gin, "New Type of Membrane Material for Water Desalination Based on a Cross-Linked Bicontinuous Cubic Lyotropic Liquid Crystal Assembly," *J. Am. Chem. Soc.*, vol. 129, pp. 9574–9575, Aug. 2007.

[24] X. Feng, M. E. Tousley, M. G. Cowan, B. R. Wiesenauer, S. Nejati, Y. Choo, R. D. Noble, M. Elimelech, D. L. Gin, and C. O. Osuji, "Scalable Fabrication of Polymer Membranes with Vertically Aligned 1 nm Pores by Magnetic Field Directed Self-Assembly," *ACS Nano*, vol. 8, pp. 11977–11986, Dec. 2014.

[25] X. Feng, S. Nejati, M. G. Cowan, M. E. Tousley, B. R. Wiesenauer, R. D. Noble, M. Elimelech, D. L. Gin, and C. O. Osuji, "Thin Polymer Films with Continuous Vertically Aligned 1 nm Pores Fabricated by Soft Confinement," *ACS Nano*, vol. 10, pp. 150–158, Jan. 2016.

[26] S. M. Dischinger, M. J. McGrath, K. R. Bourland, R. D. Noble, and D. L. Gin, "Effect of Post-Polymerization Anion-Exchange on the Rejection of Uncharged Aqueous Solutes in Nanoporous, Ionic, Lyotropic Liquid Crystal Polymer Membranes," *J. Membr. Sci.*, vol. 529, pp. 72–79, May 2017.

[27] R. Resel, G. Leising, P. Markart, M. Kriechbaum, R. Smith, and D. Gin, "Structural properties of polymerised lyotropic liquid crystals phases of 3,4,5-tris(-acryloxyalkoxy)benzoate salts," *Macromol. Chem. Phys.*, vol. 201, pp. 1128–1133, July 2000.

[28] M. O. Sinnokrot, E. F. Valeev, and C. D. Sherrill, "Estimates of the Ab Initio Limit for Interactions: The Benzene Dimer," *J. Am. Chem. Soc.*, vol. 124, pp. 10887–10893, Sept. 2002.

[29] A. Gierer and K. Wirtz, "Molekulare Theorie der Mikroreibung - Molecular Theory of Microfriction," *Z. Naturforsch*, vol. 8, pp. 532–538, 1953.

[30] H. S. Biswal, "Hydrogen Bonds Involving Sulfur: New Insights from ab Initio Calculations and Gas Phase Laser Spectroscopy," in *Noncovalent Forces* (S. Scheiner, ed.), Challenges and Advances in Computational Chemistry and Physics, pp. 15–45, Cham: Springer International Publishing, 2015.

[31] Y. Meroz, I. M. Sokolov, and J. Klafter, "Subdiffusion of Mixed Origins: When Ergodicity and Nonergodicity Coexist," *Phys. Rev. E*, vol. 81, p. 010101, Jan. 2010.

[32] Y. Meroz and I. M. Sokolov, "A Toolbox for Determining Subdiffusive Mechanisms," *Phys. Rep.*, vol. 573, pp. 1–29, Apr. 2015.

[33] C. Truong, L. Oudre, and N. Vayatis, "A Review of Change Point Detection Methods," *arXiv*, Jan. 2018. arXiv: 1801.00718.

[34] F. X. Diebold, T. A. Gunther, and A. S. Tay, "Evaluating Density Forecasts with Applications to Financial Risk Management," *International Economic Review*, vol. 39, no. 4, pp. 863–883, 1998.

[35] J. D. Hamilton, *Time Series Analysis*. Princeton University Press, 1994.